Published in final edited form as:
Phys Med Biol. 2012 November 21; 57(22): 7519–7542. doi:10.1088/0031-9155/57/22/7519.

Iterative image reconstruction for cerebral perfusion CT using pre-contrast scan induced edge-preserving prior

Jianhua Ma[1,2], **Hua Zhang**[1], **Yang Gao**[1], **Jing Huang**[1], **Zhengrong Liang**[2,3], **Qianjing Feng**[1], and **Wufan Chen**[1,3]

Jianhua Ma: jhma@smu.edu.cn

[1]Department of Biomedical Engineering, Southern Medical University, Guangdong Guangzhou, 510515, China

[2]Department of Radiology, State University of New York, Stony Brook, NY 11794, USA

Abstract

Cerebral perfusion X-ray computed tomography (PCT) imaging, which detects and characterizes the ischemic penumbra, and assesses blood-brain barrier permeability with acute stroke or chronic cerebrovascular diseases, has been developed extensively over the past decades. However, due to its sequential scan protocol, the associated radiation dose has raised significant concerns to patients. Therefore, in this study we developed an iterative image reconstruction algorithm based on the maximum a posterior (MAP) principle to yield a clinically acceptable cerebral PCT image with lower milliampere seconds (mAs). To preserve the edges of the reconstructed image, an edge-preserving prior was designed using a normal-dose pre-contrast unenhanced scan. For simplicity, the present algorithm was termed as "MAP-ndiNLM". Evaluations with the digital phantom and the simulated low-dose clinical brain PCT datasets clearly demonstrate that the MAP-ndiNLM method can achieve more significant gains than the existing FBP and MAP-Huber algorithms with better image noise reduction, low-contrast object detection and resolution preservation. More importantly, the MAP-ndiNLM method can yield more accurate kinetic enhanced details and diagnostic hemodynamic parameter maps than the MAP-Huber method.

1. Introduction

Cerebral perfusion X-ray computed tomography (PCT) imaging has been advocated to detect and characterize the ischemic penumbra, and assess blood-brain barrier permeability with acute stroke or chronic cerebrovascular diseases (Koenig *et al* 1998, Klotz *et al* 1999, Hopyan *et al* 2010). In cerebral studies, perfusion hemodynamic parameters can be calculated from the time sequence of enhanced CT images to provide important guidance to clinicians (Hoeffner *et al* 2004, Wintermark et al 2009). Currently, the standard scan protocol for PCT examination is performed as follows: First, pre-contrast unenhanced CT scan of the whole brain is performed. Then, after approximately several seconds following an intravenous injection of iodinated contrast agent, continuous enhanced scan of the selected CT slices of concern in a cine mode is performed for about 1 min. The PCT scan protocol shows that the associated excessive radiation exposure is more serious than that in the routine CT scan as reported in the literatures (Hirata *et al* 2005, Mnyusiwalla *et al* 2009) with a mean effective dose of 4.9±0.0 mSv and a mean dose length product (DLP) of 2663.6±5.0 mGy.cm. Therefore, a great concern has been raised pointing that repeated scans during PCT examination delivers the excessive radiation to patients (Frush *et al* 2003,

[3]Author to whom any correspondence should be addressed.

Imanishi *et al* 2005, Wintermark and Lev 2010). Minimizing the radiation dose in PCT is an interesting topic of ongoing research activities.

Up to now, many considerable efforts to reduce the radiation dose in PCT have been performed and several related techniques have been developed (Fleischmann *et al* 2000, Wintermark *et al* 2000, Wiesmann *et al* 2008, Yu *et al* 2009, Badea *et al* 2011, Jia *et al* 2010). Among these approaches, optimizing PCT scan protocol may be a basic and important strategy. For example, the tube voltage is usually set at 120 kVp during the pre-contrast unenhanced scan, and is changed to 80 kVp during the dynamic enhanced scan. Related approaches can significantly reduce the radiation dose without compromising quality. Another radiation dose reduction strategy is to decrease the image acquisition frequency in the enhanced scans. Meanwhile, related studies demonstrate significantly different conclusions (Wintermark *et al* 2004, Kamena *et al* 2007, Wiesmann *et al* 2008). The feasibility of reducing radiation dose by decreasing the image acquisition frequency still needs further investigation. Lower milliampere-seconds (mAs) in data acquisition may be a simple and cost-effective approach for performing low-dose PCT scan. Unfortunately, the associated data noise will unavoidably increase which usually leads to reduced image quality.

In PCT imaging, similar information among the different PCT time-frames has great similarities. A previously scanned high-quality diagnostic CT image may be used as a priori information. For example, Yu *et al* (2009) proposed a previous scan-regularized reconstruction strategy (PSRR) wherein the previous scans of the patient were used to recover the low-dose images with encouraging results. Given that the PSRR needs accurate image registration and nonlinear filtering techniques, any residual error in the image registration due to inter-fractional variation in treatment positions and deformation of the tissues/organs may cause significant error in the reconstructed images. To relieve the registration requirements, Ma *et al* (2011a) presented a low-dose CT image filtering method (named “ndiNLM” method) to utilize the previous normal-dose CT scan of the patient as a priori information to restore the signal from the current low-dose CT images. The ndiNLM method does not need accurate image registration and can effectively improve the image quality of the low-dose CT scan. In this paper, an iterative image reconstruction algorithm with the maximum a posterior (MAP) principle is developed, by incorporating a pre-contrast scan induced edge-preserving prior, to yield a clinically acceptable cerebral PCT image with lower mAs. For simplicity, the present algorithm is termed “MAP-ndiNLM”. The novelty of the MAP-ndiNLM method is two-fold. First, because the ndiNLM filter utilizes the redundancy of information in the previous normal-dose scan and further exploits ways to optimize the nonlocal weights for improving current low-dose image quality, the associative ndiNLM prior in the MAP-ndiNLM method can explore the extensively similar information in the pre-contrast normal-dose image by using optimized ndiNLM weights. Second, the MAP-ndiNLM method can relax the need for accurate registration via its patch-based search mechanism. Qualitative and quantitative evaluations were carried out on both the digital phantom and scans of clinical patients in terms of accuracy and resolution properties.

The remaining of the paper is organized as follows. Section 2 describes the CT imaging model, the present ndiNLM prior and the associated MAP-ndiNLM image reconstruction algorithm. The experiments setup and evaluation metrics are also presented in this section. In sections 3, the evaluation results are presented. Finally, the discussion and conclusion are given in section 4.

2. Methods and materials

2.1. CT imaging model

Without loss of generality, under the assumption of mono-energetic beam, the X-ray CT measurement can be approximately expressed as a discrete linear system:

$$y=H\mu \quad (1)$$

where y represents the obtained sinogram data (projections after system calibration and logarithm transformation), *i.e.,* $y = (y_1, y_2, \cdots y_M)^T$, μ is the vector of attenuation coefficients to be estimated, *i.e.,* $\mu = (\mu_1, \mu_2, \cdots \mu_N)^T$, where '$T$' denotes the matrix transpose. The operator H represents the system or projection matrix with the size of $M \times N$. The element of H_{ij} denotes the length of intersection of projection ray i with voxel j. In our implementation, the associated element was pre-calculated by a fast ray-tracing technique (Han *et al* 1999) stored as a file. The goal for CT image reconstruction is to estimate the attenuation coefficients μ from the measurement y according to the measurement model (1).

In solving μ, to invert (1) directly is difficult because the system matrix dimension is huge in current CT system and degraded seriously for image reconstruction from the measured noisy sinogram data. To address this problem, several approaches are proposed (Wang *et al* 2006, Han *et al* 2011). In this paper, we are using the penalized weighted least-squares approach based on the MAP estimation criterion (Li *et al* 2004, Wang *et al* 2006). The associated mathematical formula for MAP CT image reconstruction with a priori term $R(\mu)$ can be expressed as follows:

$$\mu^*=\arg\min_{\mu\geq 0} \left\{(y - H\mu)'\Sigma^{-1}(y - H\mu)+\beta R(\mu)\right\} \quad (2)$$

where Σ is a diagonal matrix with the i th element of σ_i^2 which is the variance of sinogram data y. β is a hype-parameter to balance the fidelity term (*i.e.*, first term of equation (2)) and priori term. In the implementation, the variance of σ_i^2 was determined by the following mean-variance relationship proposed by Ma *et al* (2012a, 2012b):

$$\sigma_i^2=\frac{1}{I_0}\exp(\bar{p}_i)\left(1+\frac{1}{I_0}\exp(\bar{p}_i)(\sigma_e^2 - 1.25)\right) \quad (3)$$

where I_0 denotes the incident X-ray intensity, $\bar{p}_i$ is the mean of the sinogram data at bin i and σ_e^2 is the background electronic noise variance.

2.2. ndiNLM prior

The priori term $R(\mu)$ in equation (2) plays an important role for successful image reconstruction. In this paper, according to the previous studies for non-local means regularization in both image deconvolution (Mignotte 2008) and PET image reconstruction (Ma *et al* 2010), we propose a normal-dose scan induced edge-preserving prior (named "ndiNLM prior"), which is expressed as:

$$R(\mu)=\phi_p(\mu - \text{ndiNLM}(\mu)) \quad (4)$$

where the ϕ_p denotes the potential function, ndiNLM(μ) represents an previous scan induced nonlocal means filter (Ma *et al* 2011a), which is defined as follows:

$$\mathrm{ndiNLM}(\mu(i))=\sum_{j\in N_i} w(i,j)\mu_{\mathrm{nd}}(j) \quad (5)$$

where N_i denotes the search-window and $\mu_{\mathrm{nd}}(j)$ denotes the image intensity at the voxel j in the reference image domain. The weight $w(i, j)$ quantifies the similarity between the voxel i in the object image μ and the voxel j in the reference image μ_{nd}, respectively, which can be expressed as follows:

$$w(i,j)=\frac{C}{Z(i)}\cdot\exp\left\{\frac{-\left\|\mu(n_i)-C\cdot\mu_{\mathrm{nd}}(n_j)\right\|_{2,\alpha}^2}{h^2}\right\} \quad (6)$$

$$Z_i=\sum_{j\in N_i}\exp\left\{\frac{-\left\|\mu(n_i)-C\cdot\mu_{\mathrm{nd}}(n_j)\right\|_{2,\alpha}^2}{h^2}\right\} \quad (7)$$

where the n_i and n_j denote two local similarity neighborhoods (named patch-windows) centered at the voxels i and j, respectively. The terms $\mu(n_i)$ and $\mu_{\mathrm{nd}}(n_j)$ denote the vector of neighborhood voxel values restricted in the patch-windows n_i and n_j, respectively. The notation $\|\cdot\|_{2,\alpha}$ denotes a Gaussian-weighted Euclidean distance between two similarity patch-windows, where α is the standard deviation of the Gaussian function (Buades *et al* 2005). In equation (6), h is a parameter controlling the decay of the exponential function.

In PCT imaging, the influence of injected contrast leads to the local enhancement of the temporal frame images. And the tube voltage and tube current in the contrast enhanced CT scans are generally different compared to those in the pre-contrast unenhanced scan. As a result, the associated CT values in several specific regions may exist significantly variation between the unenhanced and enhanced images. Given the above observations, a local compensation factor C is naturally incorporated in equation (6) to account for local intensity change.

$$C\left(\mu(n_i),\mu_{\mathrm{nd}}(n_j)\right)=\begin{cases}\frac{E(\mu(n_i))}{E(\mu_{\mathrm{nd}}(n_j))}, & E\left(\mu(n_i)-\mu_{\mathrm{nd}}(n_j)\right)\geq\sigma\\ 1, & \text{otherwise}\end{cases} \quad (8)$$

where $E(\cdot)$ denotes the expected value or mean of the intensity in the patch-window n_i, and the threshold factor σ can be determined by estimating the standard deviation of homogeneous area near the patch-window neighborhood.

Generally, the potential function $\phi_p(\cdot)$ in equation (4) could be selected to satisfy two conditions (Chan *et al* 2004), *i.e.*, (i) $\phi_p\in C$; and (ii) $\phi_p(\cdot)$ is a symmetrical convex function on any bounded interval. Specifically, in this study, to preserve edges in the reconstructed image, the following potential function is adopted (Bouman *et al* 1993):

$$\phi_p(t)=\|t\|_p^p,\ 1<p<2 \quad (9)$$

where $\|\cdot\|_p$ denotes the p-norm of the discrete magnitude of the image and p can be regarded as a shape factor which controls the cost of abrupt edges. In the implementation, p was set to 1.2 for all the cases.

In summary, the cost function in equation (2) in the image domain can be rewritten as:

$$\mu^{*}=\arg\min_{\mu\geq 0}\left\{(y-H\mu)'\sum^{-1}(y-H\mu)+\beta\|\mu-\mathrm{ndiNLM}(\mu)\|_{p}^{p}\right\}. \quad (10)$$

2.3. MAP-ndiNLM image reconstruction

Given that the weight $w(i, j)$ in equation (6) is a function of the object image μ and the reference image μ_{nd}, to solve the cost function in equation (10) according to the existing methods is difficult. Thus, in this paper, a binary optimal scheme (Ma *et al* 2010) was used to optimize the cost function in equation (9), which can automatically adjust the weight $w(i, j)$ in equation (6) according to the similarity between the patch-windows in the current estimation μ^{n} (n is the iterative index) and the normal-dose unenhanced image μ_{nd} during each iteration. The MAP-ndiNLM method for PCT image reconstruction has three main steps as follows.

1. *Prior estimation*: Given the current image estimation μ^{n} and the normal-dose unenhanced image μ_{nd}, the ndiNLM filter in (5) is first performed between μ^{n} and μ_{nd} and then the term $R(\mu)$ is calculated in (4).
2. *Steepest descent optimization*: The steepest descent scheme is utilized to yield new image estimation, *i.e.*, μ^{n+1}, which can be expressed as follows:

$$\mu^{n+1}=\mu^{n}-\alpha^{n+1}\left(H^{T}\left(\Sigma^{-1}(H\mu^{n}-y)\right)\right)-\beta R'(\mu^{n}) \quad (11)$$

   where α^{n+1} represents the gradient step-size which can be calculated adaptively by the following estimator (Sullivan *et al* 1991):

$$\alpha^{n+1}=\frac{G^{T}\mathrm{G}}{(H\mathrm{G})^{T}\ (\Sigma^{-1}(HG))}\ \text{with}\ G\triangleq H^{T}\left(\Sigma^{-1}(H\mu^{n}-y)\right) \quad (12)$$

   and

$$R'(\mu^{n})=p(1-Z^{-1})\mathrm{sign}(\mu^{n}-\mathrm{ndiNLM}(\mu^{n}))\left|\mu^{n}-\mathrm{ndiNLM}(\mu^{n})\right|^{p-1} \quad (13)$$

   where Z is the normalizing factor of the ndiNLM filter for each voxel in (5). In the implementation, because of $Z\gg 1$, let $R'(\mu^{n})\approx p\,\mathrm{sign}(\mu^{n}-\mathrm{ndiNLM}(\mu^{n}))|\mu^{n}-\mathrm{ndiNLM}(\mu^{n})|^{p-1}$.
3. *Cycle Update*: Update μ^{n+1} using the aforementioned steps in each iteration cycle.

In the implementation, the preliminary image reconstructed by the FBP method is used for setting the threshold factor σ in equation (8), and then the final reconstruction is performed using the set threshold factor σ.

2.4. Experimental data acquisitions

To evaluate the performance of the present MAP-ndiNLM for enhanced PCT image reconstruction, three modified digital Shepp-Logan phantoms and clinical brain PCT images were used in the experiments.

2.4.1. Digital Shepp-Logan phantoms—Three modified 2D Shepp-Logan phantoms are demonstrated in figure 1. Figure 1(a) shows the pre-contrast unenhanced CT image. Figure 1(b) shows the corresponding enhanced image wherein the large bright region represents the enhanced tissue. Figure 1(c) shows the enhanced image with a low-contrast lesion indicated by an arrow. Each phantom is composed by 256 × 256 square pixels with

the intensity value from 0 to 1200 HU. Table 1 lists the parameters of the ellipsoids (or objects) in the modified 2D Shepp-Logan phantom as shown in figure 1(c). The size of each pixel is 1.0 mm × 1.0 mm. We chose a geometry that was representative for a mono-energetic fan-beam CT scanner setup with a circular orbit to acquire 984 views over 2π. The number of channels per view was 888. The distance from the rotation center to the curved detector is 408 mm and the distance from the X-ray source to the detector is 949 mm. Each projection datum along a X-ray through the sectional image is computed based on the known densities and intersection areas of the ray with the geometric shapes of the objects in the sectional image.

For the sinogram data simulation, similar to the study (La Rivière *et al* 2006), after calculating the noise-free line integral y as a direct projection operation based on model (1), the noisy measurement b_i at each bin i was generated according to the statistical model of pre-logarithm projection data:

$$b_i=\text{Poisson}(I_0\exp(-y_i))+\text{Normal}(0,\sigma_e^2) \quad (14)$$

where I_0 denotes the incident X-ray intensity and σ_e^2 is the background electronic noise variance. In the present study, the X-ray exposure level I_0 was set to 2.5×10^5 and σ_e^2 was set to 10 for low-dose scan simulation. The noisy measurement y_i was calculated by the logarithm transform of b_i.

2.4.2. Clinical cerebral PCT data—Clinical cerebral PCT images of a patient with an old infarction were acquired with a 64-slice multi-detector CT (MDCT) scanner from Siemens without table movement. First, a pre-contrast unenhanced scan of the whole brain was performed with a tube current of 240 mA, tube voltage of 80 kVp. Then, 50 ml of Iopromide 30 370 (Ultravist, Schering, Germany) was injected at a rate of 5.0 ml/s. The cine (continuous) enhanced normal-dose scan was performed by the following protocol: 200 mA, 80 kVp, slice thickness 8.0 mm, 1 s per rotation for duration of 39 s, and reconstruction kernel of H30s. The parameters of scanning imaging were as follows: (1) each rotation included 1160 projection views evenly spaced on a circular orbit; (2) each view contained 672 data elements each from one of the 672 detector bins; (3) the source-to-detector distance was 1040 mm; (4) The source-to-isocenter distance was 570 mm; and (5) the space of each detector bin was 0.6 mm.

To reduce radiation dose, instead of scanning the patient twice, we simulated the low-dose cerebral perfusion enhanced CT sinogram data by the simulation method (La Rivière *et al* 2006) described in subsection of 2.4.1 from the acquired normal-dose enhanced images which were used as the digital phantom data based on the above described Siemens 64-slice MDCT imaging parameters. The CT dose index (CTDIvol) for the normal-dose enhanced scan is 380.80 mGy. The CTDI_{vol} for the simulated low-dose contrast-enhanced CT data is about one-seventh of that from the normal-dose scan.

2.5. Performance evaluation

2.5.1. Evaluation by noise reduction—The following three metrics were utilized to evaluate the noise reduction for the quantitative comparison: (1) local signal to noise ratio (lSNR); (2) mean per cent squared error (MPSE); and (3) mean per cent absolute error (MPAE):

$$\mathrm{lSNR}=\frac{\frac{1}{Q}\sum_{m=1}^{Q}\mu(m)}{\sqrt{\frac{1}{Q}\sum_{m=1}^{Q}\left(\mu(m)-\frac{1}{Q}\sum_{m=1}^{Q}\mu(m)\right)^{2}}} \quad (15)$$

$$\mathrm{MPSE}=\frac{100}{\bar{\mu}_{\mathrm{xtrue}}(m)}\sqrt{\frac{1}{Q-1}\sum_{m=1}^{Q}[\mu(m)-\mu_{\mathrm{xtrue}}(m)]^{2}} \quad (16)$$

$$\mathrm{MPAE}=\frac{100}{Q}\sum_{m=1}^{Q}\left|\frac{\mu(m)}{\mu_{\mathrm{xtrue}}(m)}-1\right| \quad (17)$$

where $\mu(m)$ denotes the voxel value of estimated low-dose image, $\mu_{\mathrm{xtrue}}(m)$ and $\bar{\mu}_{\mathrm{xtrue}}(m)$ denote the voxel value and the associated average voxel value in the region of interest (ROI) of normal-dose image, Q is the total number of voxels in the ROI.

2.5.2. Noise-resolution tradeoffs—The noise-resolution tradeoff curves from the FBP, MAP-Huber and MAP-ndiNLM methods were generated from the simulated sinogram data using the modified Shepp-Logan phantom in figure 1(b). Image reconstruction was performed on a 256×256 array size. The image resolution was analyzed by the edge spread function (ESF) along the vertical profile as indicated by a line in figure 1(b). Based on the strategy described in (La Rivière and Billmire 2005), assuming the broadening kernel is a Gaussian function with standard deviation δ_b, an error function (erf) can be used to represent the ESF function parameterized by δ_b. Consequently, the parameter δ_b can be calculated by fitting the vertical profile to the error function, and the associated full-width at half-maximum (FWHM) of the Gaussian broadening kernel can be denoted as $2.35\,\delta_b$ which is used to indicate the resolution of the reconstructed image. In this study, the noise level of the reconstructed image was characterized by the standard deviation of a uniform region of size 19×19 in the background region around the large bright region. Since the reconstruction kernel of FBP method significantly influences the image quality, the associative images were reconstructed by using the different Hanning filters with the Nyquist frequency cut-off from 90% to 50%. By varying the penalty parameter β for the MAP-ndiNLM from 2.0×10^{-4} to 2.5×10^{-3} and for the MAP-Huber from 2.0×10^{3} to 2.5×10^{4}, we obtained the corresponding noise-resolution tradeoff curves as illustrated in figure 4.

2.5.3. Receiver operating characteristic study—The ability of lesion detection is a general principle for evaluating the performance of a medical imaging system. Receiver operating characteristic (ROC) curve may provide a most comprehensive description as they indicate all of the combinations of sensitivity and specificity in a diagnostic test. In practice, a variety of pairs of true positive fraction (TPF) and false positive fraction (FPF) can be first generated, and then ROC curve can be drawn or fitted from the obtained TPF and FPF (Metz 1986). The diagnostic accuracies indicated by these curves can be ranked unambiguously in terms of the total area under each curve within the unit square. The associated area index is often named as “AUC”. In CT image reconstruction, larger AUC usually reflects better lesion detectability. To eliminate the intra human observer variation, the channelized Hotelling observer (CHO) was usually employed to generate the ROC curves (Myers and Barrett 1987). The series of ratings from the output were subsequently analyzed using the ROCKIT package with bi-normal model (http://metz-roc.uchicago.edu/). In this paper, ROC

studies were performed from the computer-generated datasets by adding a low-contrast small lesion (5% higher than background intensity) in a modified Sheep-Logan phantom as indicated by an arrow in Figure 1(c). To evaluate the ability of lesion detection of the MAP-ndiNLM method, a total of 100 noisy sinogram data were generated according to equation (14) using the Shepp-Logan phantom with and without the low-contrast region. The associated images were reconstructed by the FBP, MAP-Huber and MAP-ndiNLM methods from the same noisy sinogram data, respectively.

2.5.4. Time density curves study—The estimation of hemodynamic functional parameters is obtained from the measurement of the temporal evolution of the concentration of contrast agent at each pixel position in the ROI. The associated temporal evolution can be denoted by time density curve (TDC). However, the noise in the individual time frame images would produce negative influence in the calculation of the TDCs. Thus, curve fitting (like the gamma fit) is often used in TDC calculation. In this study, to make the evaluation more intuitive, the curve fitting was not adopted and the rough TDCs were directly calculated from the reconstructed sequential images.

2.5.5. Hemodynamic parameters evaluation—Another main goal of PCT imaging is to achieve the functional hemodynamic parameters, which reflects the blood supply. In our studies, cerebral blood volume (CBV), cerebral blood flow (CBF) and mean transit time (MTT) maps were calculated by using a free software program, Perfusion Mismatch Analyzer (PMA) software (Kudo 2009). As a standardize software, PMA was developed in the activity of Acute Stroke Imaging Standardization group in Japan. A standard singular-value decomposition method was used with the PMA for perfusion parameter calculation in our study.

2.6. Other experiments settings

To validate and evaluate the performance of the present MAP-ndiNLM method, the FBP method using the Hanning filter with cutoff at 80% Nyquist frequency and the MAP-Huber method described in (Wang *et al* 2009) were adopted for comparison. The MAP-Huber was implemented by incorporating the following penalty term:

$$R(\mu)=\sum_i \sum_{j\in S_i} w_{ij}\phi(\mu_i-\mu_j) \quad (18)$$

where the weight w_{ij} is a positive value that denotes the interaction degree between the pixels i and j, S_i is a local neighborhood. The associative Huber potential function is given as follows:

$$\phi(t)=\begin{cases} t^2/2, & |t|\le\delta \\ \delta|t|-\delta^2/2, & |t|>\delta \end{cases} \quad (19)$$

where δ is a threshold parameter. The Huber potential function penalizes the difference between neighboring pixels if the absolute difference pixel value $|t|$ is smaller than some threshold δ and it will apply a linear penalty to the large difference of $|t|>\delta$ which usually occurs at edges.

The related parameters in the implementation were selected as follows: For the MAP-ndiNLM, (1) the size of the "search-window" N_i was 23 × 23; (2) the size of the "patch-window" n was 5 × 5; (3) the standard deviation α of the Gaussian function was 1; (4) the parameters h and β were selected for different cases by visual inspection. And for the MAP-Huber, (1) the weight w_{ij} was 1 for first-order neighbors and $1/\sqrt{2}$ for second-order

neighbors; (2) the threshold δ was 0.1; (3) the parameter β was selected for different cases by visual inspection. All the algorithms were implemented in Matlab 7.9 (The Math Works, Inc.) programming environment. The codes were run on a typical desktop computer with AMD Phenom (TM) II X6 1055T Processor, 2.80 GHz and 16GB of RAM memory.

3. Results

3.1. Digital phantom studies

Figure 2 shows the results reconstructed by different methods. Figure 2(a) shows the noise-free Shepp-Logan phantom image, which serves as a "ground truth" for comparison. Figure 2(b) shows the image reconstructed by the FBP method from the noisy sinogram data. Serious noise-induced artifacts can be observed. Figure 2(c) shows the image reconstructed by the MAP-Huber method from the noisy sinogram data. Noise-induced artifacts were suppressed successfully, but some new artifacts can be observed in the background region. Figure 2(d) shows the image reconstructed by the MAP-ndiNLM method from the noisy sinogram data. The MAP-ndiNLM method can not only significantly suppress the noise-induced streak artifacts, but also greatly preserve the edge structure information. Furthermore, the profiles in figure 3 demonstrates that the MAP-ndiNLM achieves more noticeable gains than the MAP-Huber in preserving the edge details as indicated by the three arrows in figure 3(b). To evaluate the MAP-ndiNLM method quantitatively, the noise reduction, noise-resolution tradeoffs and ROC curve were measured in the following subsections.

3.1.1. Noise reduction measurement—Table 2 lists the lSNR, MPSE and MPAE metrics of three ROIs derived from the low-dose CT reconstructions by three different methods. The results from both the MAP-ndiNLM and the MAP-Huber methods exhibit significant gains over the FBP method in terms of the three metrics. Moreover, the MAP-ndiNLM method performs better than the MAP-Huber method with more than 7%, 56%, and 21% gains of lSNR in three different ROIs, respectively. The MPSE, MPAE metrics also further demonstrate better performance of the present MAP-ndiNLM approach than other two methods with smaller metric values in three ROIs.

3.1.2. Noise-resolution tradeoffs—Figure4 shows the noise-resolution curves of different methods. We can see the noise-resolution curves from the FBP, MAP-Huber and MAP-ndiNLM methods have similar trends, but the MAP-ndiNLM method shows better performance than the FBP and MAP-Huber methods in terms of the noise-resolution tradeoff curve.

3.1.3. ROC curve—Figure 5 shows the ROC curves from the FBP, MAP-Huber and MAP-ndiNLM methods. The area under the ROC curve from the MAP-ndiNLM method is 0.8605 whereas the areas under the ROC curve from the MAP-Huber and FBP methods are 0.8283, 0.7669, respectively. The results indicate that the MAP-ndiNLM method slightly outperforms the FBP and MAP-Huber methods in terms of detectability of abnormality in low-contrast diagnosis.

3.2.Clinical studies

Figure 6(a) shows the original pre-contrast unenhanced scan image which acts as the reference image for the MAP-ndiNLM method. Figure 6(b) shows the normal-dose enhanced image which is used as a golden standard for comparison. Figure 6(c) shows the simulated low-dose enhanced image reconstructed by the FBP method wherein serious noise-induced artifacts can be observed, which obscure the enhancement information. Figure 6(d) shows the low-dose enhanced image reconstructed by the MAP-Huber method. Lastly,

figure 6(e) shows the low-dose enhanced image reconstructed by the MAP-ndiNLM method. The clearly delineated and enhanced signal in the MAP-ndiNLM image is better reproduced than that from the MAP-Huber method with the edge preservation and noise suppression. However, from the zoomed images displayed in the right bottom corners, it can be seen that compared to the normal-dose FBP image, the MAP-ndiNLM method yields result with little loss of spatial resolution. Figure 7 depicts the horizontal profiles of the images in figure 6, wherein one from the normal-dose image is regarded as a golden standard. The profile from the MAP-ndiNLM method matches well with that from the normal-dose image. In other words, the gains from the present MAP-ndiNLM method are more noticeable than those from the MAP-Huber method.

3.2.1. Time density curves measurement—Figure 8 depicts the TDC accuracy of the arterial input function (AIF), venous output function (VOF) and tissue perfusion of dynamic images reconstructed from the noisy sinogram data. It can be observed that the TDCs of the AIF and VOF from the low-dose reconstructions by three methods match well with the ones from the normal-dose FBP image as shown in figure 8(a) and 8(d) because the contrast agent flow in the enhanced CT value is higher enough in such large vessels than that in the tissue and small vessels. The main aim of PCT imaging is to reconstruct the signal values within the “tissue bed”. Typical results for such regions are shown in figure 8(b) and 8(c) wherein the ROIs exclude the areas containing major blood vessel branches and suspected abnormal signs. It can be observed that the TDCs from the reconstructed images by the MAP-Huber and MAP-ndiNLM algorithms exhibit better match with ones from the normal-dose FBP image than those from the low-dose FBP reconstructions. Furthermore, the MAP-ndiNLM method works slight better than the MAP-Huber method.

To quantitatively measure the consistency between the TDCs from the normal-dose FBP images and the TDCs from the simulated low-dose images reconstructed by the FBP, MAP-Huber MAP-ndiNLM methods, table 3 lists the Lin’s concordance correlation (Ma *et al* 2012b) coefficients of four 3×3 ROIs indicated by the squares in figure 6(b). The results demonstrate that well consistency between the TDCs from the simulated low-dose FBP images and the normal-dose FBP images can be found in both the AIF and VOF regions with the Lin’s concordance correlation coefficients higher than 0.95. However, in the tissue 2, Lin’s concordance correlation coefficient from the low-dose FBP images is below than 0.7 while the corresponding Lin’s concordance correlation coefficient from the reconstructed images by the present MAP-ndiNLM method is higher than 0.9, even in cases where all lower bounds of the 95% confidence interval of the concordance correlation coefficients are higher than 0.86. In other words, the results may suggest a significant agreement between the TDCs from the MAP-ndiNLM images and the normal-dose images.

3.2.2. Hemodynamic parameters maps measurement—Figure 9 shows the perfusion parameters maps calculated from the original normal-dose images and the low-dose images reconstructed by different methods from the noisy sinogram data which related to about one-seventh radiation dose of the normal-dose scan. The MTT should be first analyzed because it shows the most prominent regional abnormalities and facilitates depiction of the ischemic area. It can be observed that the MTT map (column one) derived from the MAP-ndiNLM method is similar with that derived from the original normal-dose images. For the CBF (column two) and CBV (column three) maps, the MAP-ndiNLM method can yield sharper edges and higher contrast between gray and white matter than the conventional FBP and MAP-Huber methods. To further show the performance of the present MAP-ndiNLM method, the zoomed ROIs of the MTT, CBF and CBV maps are shown in figure 10. The results clearly demonstrate that the MAP-ndiNLM method get more gians than the FBP and MAP-Huber methods in preserving dynamic detail information, which further indicates more reliable cerebral perfusion parameters.

To demonstrate the merits of the present MAP-ndiNLM method quantitatively, we manually selected 20 specific ROIs in figure 6(b) which exclude the areas that contain major blood vessel branches and suspected abnormal signs. The ROIs were located at both hemispheres in grey matter, white matter and basal ganglia. Figure 11 illustrates the correlation coefficients, regression equation and corresponding Bland-Altman plots of MTT values in different conditions. It can be seen that the correlation coefficient derived from the normal-dose images and the low-dose image reconstructed by the MAP-ndiNLM method is higher than that from the low-dose images of other methods, whereas the difference in the ordinate axis on the Bland-Altman plot smaller. Figures 12 and 13 provide similar results from the CBV and CBF parameters. However, it is worth to mention that for the CBF parameters in figure 13 the bias from MAP-ndiNLM method is more than those from both the FBP and MAP-Huber methods. Thus, extensive study using more patients with various types of ischemic diseases should be performed to enhance the CBF parameter calculation reliability. Nevertheless, these figures may partially suggest that the MAP-ndiNLM method can achieve noticeable performance in low-dose PCT image reconstruction with the accuracy of diagnostic physiological parameters.

4. Conclusion and discussion

In this paper, we present a normal-dose enhanced scan induced edge-preserving prior for cerebral PCT iterative image reconstruction based on the MAP principle. The experimental results show that the present MAP-ndiNLM method can yield more significant performance gains than the existing MAP-Huber method in terms of different measurement metrics.

The penalty prior reflects the information of the desired CT image. The traditional edge-preserving priors usually extract information in a local neighborhood of the estimated image. In general, given that the homogeneous regions with sharp boundaries compose the desired CT image with a low noise level, these priors might work well. Meanwhile, given that the noise level is relatively significant and no clear separation of homogeneous regions exists in the desired CT image, these priors would tend to produce the so-called staircase effect. More importantly, such condition is dangerous in clinical situation because the related staircase effect may be misinterpreted as certain nonexistent objects. In PCT imaging, the pre-contrast unenhanced CT scan is executed before the enhanced CT scans. The normal-dose high-quality unenhanced CT images provide strong a priori information of the patient and it would be a natural choice for using the normal-dose unenhanced CT image to induce PCT iterative image reconstruction from the measured noisy data. However, the contrast agent used and the tissue deformation make such application challenging. Thus, to fully use the pre-contrast unenhanced CT images of the same patient, dedicated image registration techniques are needed. As discussed in detail previously (Ma *et al* 2011a), the ndiNLM filter may be a good candidate to use the previous scanned CT image for current image estimation because it does not heavily depend on the accuracy of the image registration. Consequently, an important novelty of the present MAP-ndiNLM method in this paper is the utilization of the pre-contrast normal-dose images without needing accurate image registration. In other words, the MAP-ndiNLM method can relax the need for accurate image registration processing through its patch-based search mechanism during the reconstruction process.

As for the present ndiNLM prior and the corresponding PCT iterative image reconstruction algorithm, we would like to make the following discussions. First, as a version of the widely-used one-step-late (OSL) iteration algorithm, the present ndiNLM prior based steepest descent algorithm can be feasibly and effectively implemented using the binary optimal reconstruction strategy (Ma *et al* 2010). However, given that the weight $w(i, j)$ in equation (6) depend on the unknown enhanced CT image intensity and the pre-contrast unenhanced CT image intensity, to guarantee the convex of ndiNLM prior in the whole

optimization is difficult. Similar with many existing OSL algorithms whose global convergence is an open issue, the present algorithm also suffers from the lack of strict global convergence proof. Meanwhile, even without a guarantee of global convergence, our practical experiments suggest that the present algorithm is still effective in practice for searching at least a local maximum similar to the strategy proposed by Mignotte (2008).

As one disadvantage of the present algorithm, four parameters should be selected manually, namely, the search-window N_j, the patch-window n_i, the control parameter h and the hyper-parameter β. It is worth to mention that all the related parameters are likely dependent on the application and the prescribed FOV in practice use. As for the ndiNLM prior construction, the search-window N_j should be sufficiently large to acquire more similarity information while minimizing the influence of the mismatched tissues. In our present study, by extensive experiments with visual inspection and quantitative measurements, we found that a 2 3×2 3 search-window and a 5×5 patch-window are adequate for effective noise and artifacts suppression while retaining computational efficiency. For the parameters h and β, in this paper, we briefly fixed the sizes of the search-window and patch-window and did not consider methods for optimizing them adaptively, but instead we studied the results obtained by a broad range of parameter values by hand in term of visual inspection and quantitative measurements. This scheme can also be considered as a process of trial and error. More theoretical insight in optimizing the parameters is necessary, which may be a topic for future research.

Another major drawback of the present MAP-ndiNLM algorithm is its computational burden, especially in the 3D case, as it contains the nidNLM filtration step comparing with the MAP-Huber algorithm. For example, in the case of 2D image reconstruction, given a 23×23 search-window and a 5×5 patch-window, the MAP-ndiNLM algorithm takes about 0.8 min to finish one iteration to reconstruct the image of size 512×512 using a PC with 2.80 GHz CPU. Meanwhile, the corresponding reconstruction time of MAP-Huber algorithm for one iteration is about 0.6 min. However, several techniques presented by Coupe´ *et al* (2008) can be used to reduce the computational complexity for the ndiNLM prior construction including the optimal voxel selection in the search-window, block-wise implementation, and parallel computation. In addition, with the development of fast computers and dedicated hardwares (Xu and Mueller 2005), iterative reconstruction algorithm may be used for clinical CT image reconstruction in the near future.

In this work, our effort was focused on the noise suppression of PCT image reconstruction using the iterative reconstruction algorithm. In clinics, the present method can be applied in other applications in which a high quality prior image is acquired and subsequent scans are performed, such as puncture and radiotherapy. Therefore, the present method can be adapted to the associated applications for radiation dose reduction, which may be another topic for future research.

Acknowledgments

This work was partially supported by the National Natural Science Foundation of China under grand (No. 81000613, No. 81101046), the National Key Technology Research and Development Program of the Ministry of Science and Technology of China under grant (No. 2011BAI12B03), the Science and Technology Program of Guangdong Province of China under grant (No. 2011A030300005, No. 2011YQ03011404), and the 973 Program of China under grant (No. 2010CB732503). Z. Liang and J. Ma also were partially supported by the NIH/NCI under Grant #CA143111 and Grant #CA082402.

References

Badea CT, Johnston SM, Qi Y, Johnson GA. 4D micro-CT for cardiac and perfusion applications with view under sampling. Phys. Med. Biol. 2011; 56:3351–3369. [PubMed: 21558587]

Bouman C, Sauer K. A Generalized Gaussian Image Model for Edge-Preserving MAP Estimation. IEEE Trans. Image Process. 1993; 2:296–310. [PubMed: 18296219]

Buades A, Coll B, Morel JM. A nonlocal algorithm for image denoising. Proc. IEEE Computer Vision and Pattern Reconization. 2005; 2:60–65.

Chan RH, Ho CW, Nikolova M. Convergence of Newton's method for a minimization problem in impulse noise removal. J. Comp. Math. 2004; 22:168–177.

Coupe P, Yger P, Prima S, Hellier P, Kervrann C, Barillot C. An optimized blockwise nonlocal means denoising filter for 3-D magnetic resonance images. IEEE Trans. Med. Imaging. 2008; 27:425–441. [PubMed: 18390341]

Fleischmann D, Rubin GD, Bankier AA, Hittmair K. Improved uniformity of aortic enhancement with customized contrast medium injection protocols at CT angiography. Radiology. 2000; 214:363–371. [PubMed: 10671582]

Frush DP, Donnelly LF, Rosen NS. Computed tomography and radiation risks: What pediatric health care providers should know. Pediatrics. 2003; 112:951–957. [PubMed: 14523191]

Han G, Liang Z, You J. A fast ray-tracing technique for TCT and ECT studies. IEEE Nuclear Science Symposium Conf. Record. 1999; 3:1515–1518.

Han X, Bian J, Eaker DR, Kline TL, Sidky EY, Ritman EL, Pan X. Algorithm-enabled low-dose micro-CT imaging. IEEE Trans. Med. Imaging. 2011; 30:606–620. [PubMed: 20977983]

Hirata M, Sugawara Y, Fukutomi Y, Oomoto K, Murase K, Miki H, Mochizuki T. Measurement of radiation dose in cerebral CT perfusion study. Radiat. Med. 2005; 23:97–103. [PubMed: 15827526]

Hoeffner EG, Case I, Jain R, Gujar SK, Shah GV, Deveikis JP, Carlos RC, Thompson BG, Harrigan MR, Mukherji SK. Cerebral perfusion CT: technique and clinical applications. Radiology. 2004; 231:632–644. [PubMed: 15118110]

Hopyan J, Ciarallo A, Dowlatshahi D, Howard P, John V, Yeung R, Zhang L, Kim J, MacFarlane G, Lee TY, Aviv RI. Certainty of stroke diagnosis: incremental benefit with CT perfusion over noncontrast CT and CT angiography. Radiology. 2010; 255:142–153. [PubMed: 20308452]

Imanishi Y, Fukui A, Niimi H, Itoh D, Nozaki K, Nakaji S, Ishizuka K, Tabata H, Furuya Y, Uzura M. Radiation-induced temporary hair loss as a radiation damage only occurring in patients who had the combination of MDCT and DSA. Eur. Radiol. 2005; 15:41–46. [PubMed: 15351903]

Jia X, Lou Y, Dong B, Tian Z, Jiang S. 4D computed tomography reconstruction from few-projection data via temporal non-local regularization. Medical Image Computing and Computer-Assisted Intervention. 2010; 13:143–150. [PubMed: 20879225]

Kamena A, Streitparth F, Grieser C, Lehmkuhl L, Jamil B, Wojtal K, Ricke J, Pech M. Dynamic perfusion CT: optimizing the temporal resolution for the calculation of perfusion CT parameters in stroke patients. Eur. J. Radiol. 2007; 64:111–118. [PubMed: 17383135]

Klotz E, König M. Perfusion measurements of the brain: using dynamic CT for the quantitative assessment of cerebral ischemia in acute stroke. Eur. J. Radiol. 1999; 30:170–184. [PubMed: 10452715]

Koenig M, Klotz E, Luka B, Venderink DJ, Spittler JF, Heuser L. Perfusion CT of the brain: diagnostic approach for early detection of ischemic stroke. Radiology. 1998; 209:85–93. [PubMed: 9769817]

Kudo, K. Perfusion Mismatch Analyzer (PMA). ASIST-Japan. 2009. *web site*:http://asist.umin.jp/index-e.htm

La Rivière PJ, Bian J, Vargas PA. Penalized-likelihood sonogram restoration for computed tomography. IEEE Trans. Med. Imaging. 2006; 25:1022–1036. [PubMed: 16894995]

La Rivière PJ, Billmire DM. Reduction of noise-induced streak artifacts in x-ray computed tomography through spline-based penalized-likelihood sinogram smoothing. IEEE Trans. Med. Imaging. 2005; 24:105–111. [PubMed: 15638189]

Li T, Li X, Wang J, Wen J, Lu H, Hsieh J, Liang Z. Nonlinear sinogram smoothing for low-dose X-ray CT. IEEE Trans. Nucl. Sci. 2004; 51:2501–2513.

Ma J, Feng Q, Feng Y, Huang J, Chen W. Generalized Gibbs priors based positron emission tomography reconstruction. Comput. Biol. Med. 2010; 40:565–571. [PubMed: 20447619]

Ma J, Hunag J, Feng Q, Zhang H, Lu H, Liang Z, Chen W. Low-dose computed tomography image restoration using previous normal-dose scan. Med. Phys. 2011a; 38:5713–5731. [PubMed: 21992386]

Ma, J.; Tian, L.; Huang, J.; Fan, Y.; Yu, G.; Lu, H.; Chen, W.; Liang, Z. Low-dose CT image reconstruction by α-divergence constrained total variation minimization. Proc; 11th International Meeting on Fully Three-Dimensional Image Reconstruction in Radiology and Nuclear Medicine; 2011b. p. 439-442.

Ma J, Liang Z, Fan Y, Liu Y, Huang J, Li L, Chen W, Lu H. Variance estimation of x-ray CT singoram in radon domain. Proc. SPIE. 2012a; 8313:83132G-1–83132G-8.

Ma J, Liang Z, Fan Y, Liu Y, Huang J, Chen W, Lu H. Variance analysis of x-ray CT sinograms in the presence of electronic noise background. Med. Phys. 2012b; 39:4051–4065. [PubMed: 22830738]

Metz CE. ROC Methodology in Radiological Imaging. Invest. Radiol. 1986; 21:720–733. [PubMed: 3095258]

Mignotte M. A non-local regularization strategy for image deconvolution. Pattern Recognit. Lett. 2008; 29:2206–2212.

Mnyusiwalla A, Aviv RI, Symons SP. Radiation dose from multidetector row CT imaging for acute stroke. Neuroradiology. 2009; 51:635–640. [PubMed: 19506845]

Myers KJ, Barrett HH. Addition of a channel mechanism to the ideal-observer model. J. Opt. Soc. Am. A. 1987; 4:447–457.

Sullivan BJ, Chang HC. A generalized landweber iteration for illconditioned signal restoration. Prof. IEEE Acoustics, Speech, and Signal Processing. 1991:1729–1732.

Wang J, Li T, Lu H, Liang Z. Penalized weighted least-squares approach to sinogram noise reduction and image reconstruction for low-dose X-ray computed tomography. IEEE Trans. Med. Imaging. 2006; 25:1272–1283. [PubMed: 17024831]

Wang J, Li T, Xing L. Iterative image reconstruction for CBCT using edge-preserving prior. Med. Phys. 2009; 36:252–260. [PubMed: 19235393]

Wiesmann M, Berg S, Bohner G, Klingebiel R, Schopf V, Stoeckelhuber BM, Yousry I, Linn J, Missler U. Dose reduction in dynamic perfusion CT of the brain: effects of the scan frequency on measurements of cerebral blood flow, cerebral blood volume, and mean transit time. Eur. Radiol. 2008; 18:2967–2974. [PubMed: 18618120]

Wintermark M, Lev MH. FDA investigates the safety of brain perfusion CT. Am. J. Neuroradiology. 2010; 31:2–3.

Wintermark M, Maeder P, Verdun FR, Thiran JP, Valley JF, Schnydera P, Meuli R. Using 80 kVp versus 120 kVp in perfusion CT measurement of regional cerebral blood flow. Am. J. Neuroradiology. 2000; 21:1881–1884.

Wintermark M, Rowley HA, Lev MH. Acute stroke triage to intravenous thrombolysis and other therapies with advanced CT or MR imaging: pro CT. Radiology. 2009; 251:619–626. [PubMed: 19474369]

Wintermark M, Smith WS, Ko NU, Quist M, Schnyder P, Dillon WP. Dynamic perfusion CT: optimizing the temporal resolution and contrast volume for calculation of perfusion CT parameters in stroke patients. Am. J. Neuroradiology. 2004; 25:720–729.

Xu F, Mueller K. Accelerating popular tomographic reconstruction algorithms on commodity PC graphics hardware. IEEE Trans. Nucl. Sci. 2005; 52:654–663.

Yu H, Zhao S, Hoffman EA, Wang G. Ultra-low dose lung CT perfusion regularized by a previous scan. Acad. Radiol. 2009; 16:363–373. [PubMed: 19201366]

Yu L, Liu X, Leng S, Kofler JM, Ramirez-Giraldo JC, Qu M, Christner J, Fletcher JG, McCollough CH. Radiation dose reduction in computed tomography: techniques and future perspective. Imaging Med. 2009; 1:65–84. [PubMed: 22308169]

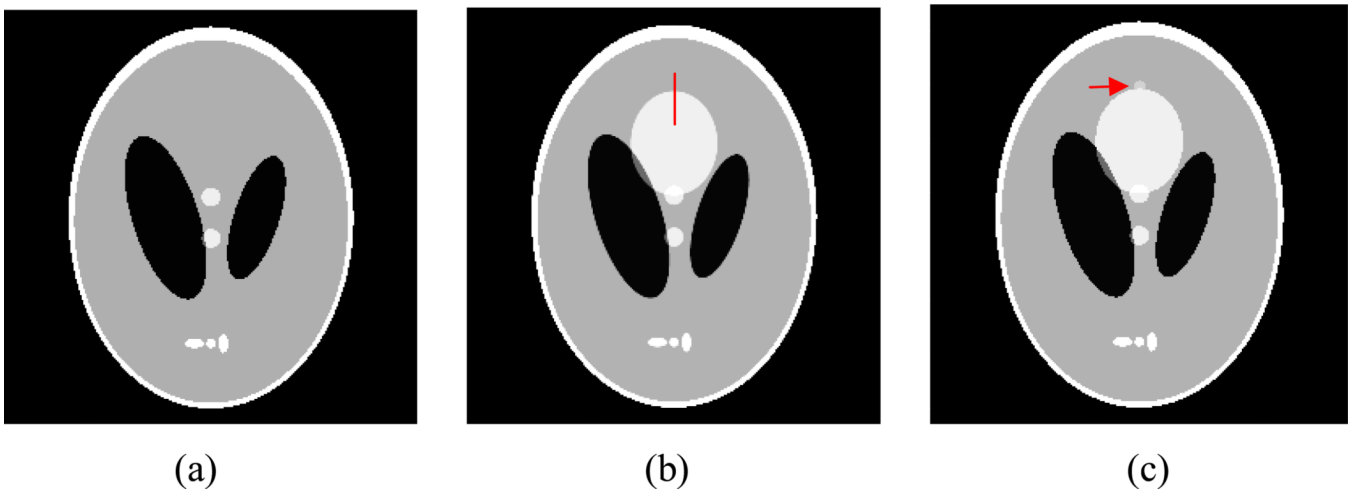

Figure 1.
Three Shepp-Logan phantoms used in the studies. (a) the pre-contrast unenhanced phantom; (b) the enhanced phantom wherein the large bright region represents the enhanced tissue; and (c) the enhanced phantom with a low-contrast lesion indicated by an arrow. The display window option: width is 220 HU, level is 670 HU.

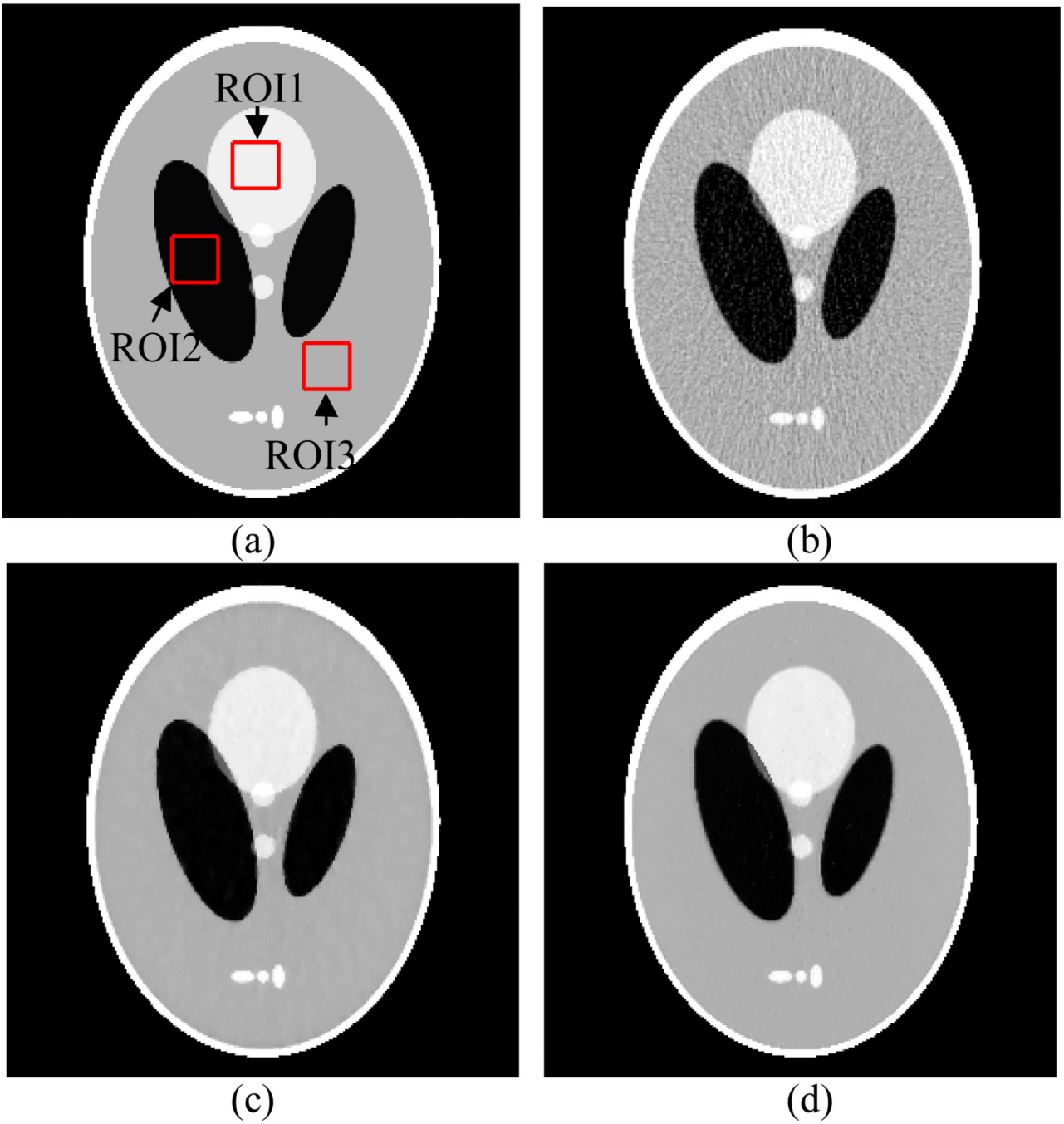

Figure 2.
Shepp-Logan phantom reconstructions by different methods. (a) the noise-free phantom image; (b) the image reconstructed by the FBP method from the noisy sinogram data; (c) the image reconstructed by the MAP-Huber method from the noisy sinogram data ($\beta = 8.0\times10^{3}$); and (d) the image reconstructed by the MAP-ndiNLM method from the noisy sinogram data (h =40.0; $\beta = 1.5\times10^{-3}$). The display window option: width is 220 HU, level is 670 HU.

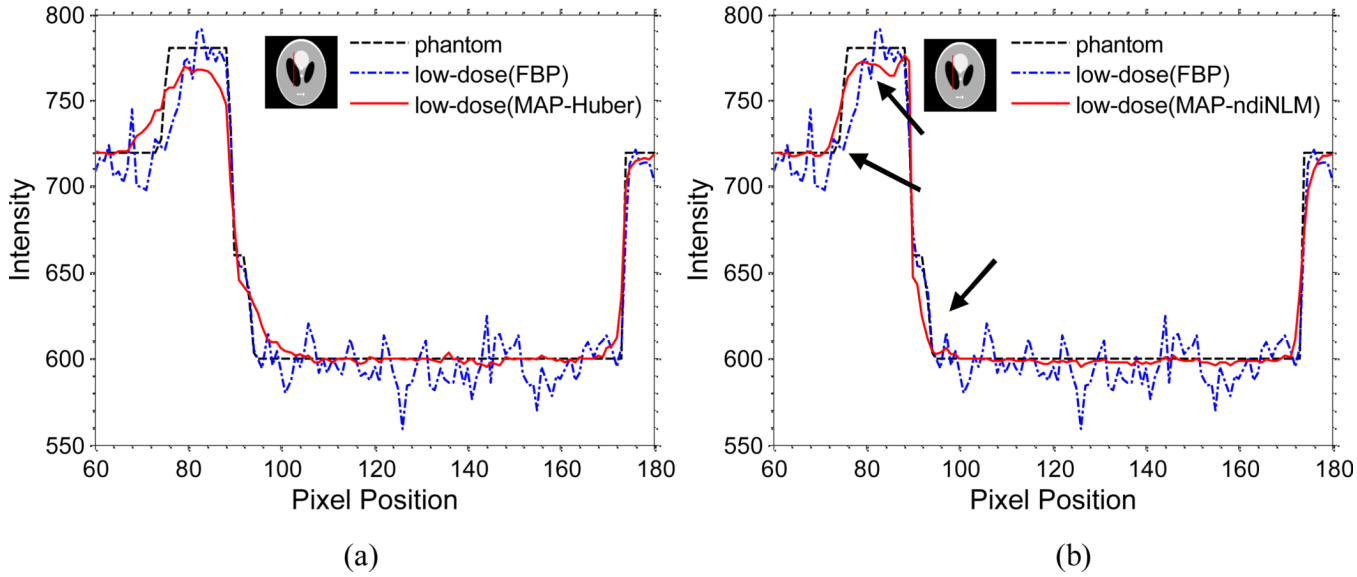

Figure 3.

Vertical profiles located at the pixel positions x =103 and y from 60 to 180 of images in figure 2. The 'blue line' is image reconstructed by the FBP method while the 'red line' is from the image reconstructed by the MAP-ndiNLM and MAP-Huber methods, respectively, and the "dotted black line" is from the noise-free phantom which acts as a ground-truth.

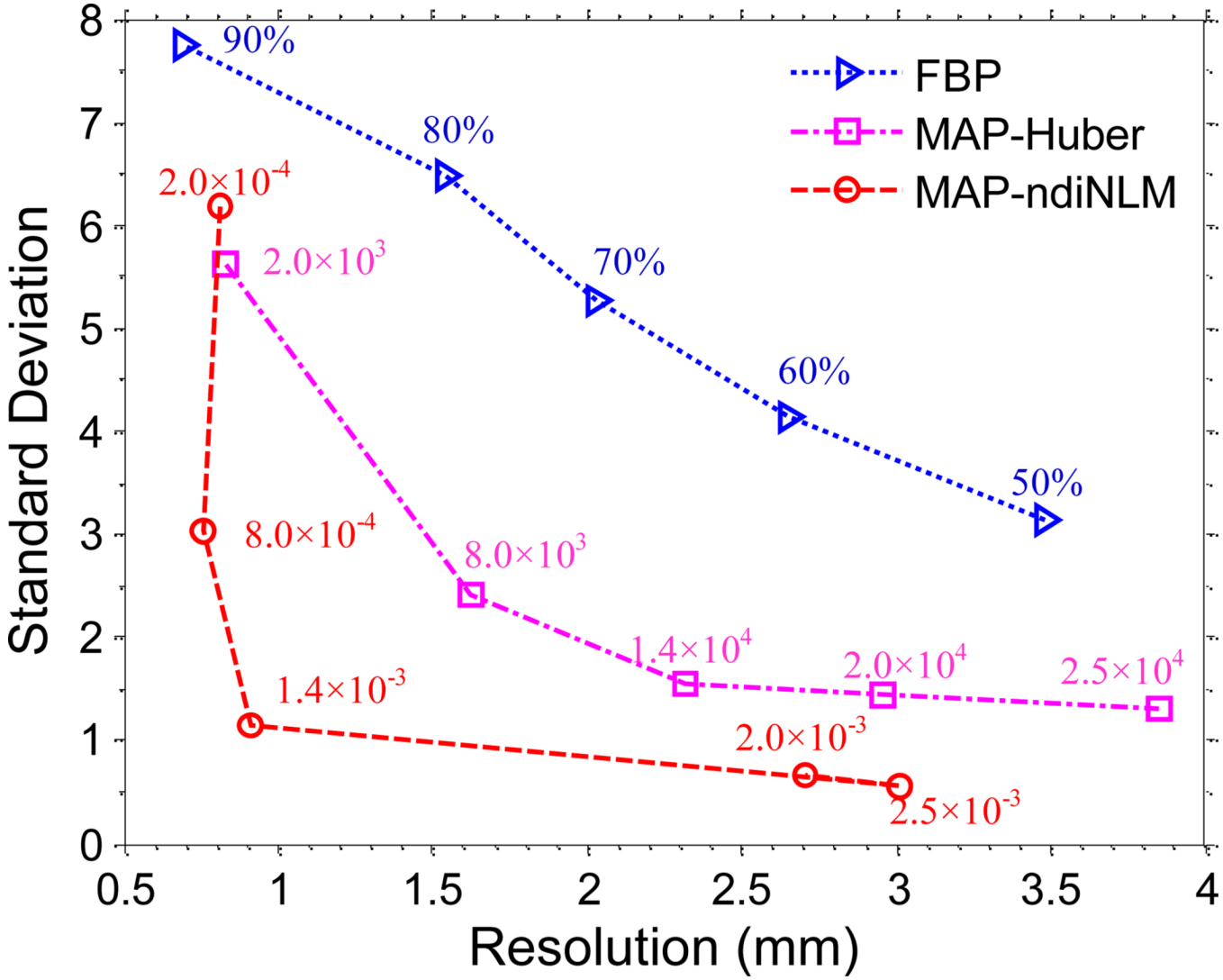

Figure 4.
The noise-resolution tradeoff curves of the FBP, MAP-Huber and MAP-ndiNLM methods. The resolution was measured by the FWHM in pixel unit.

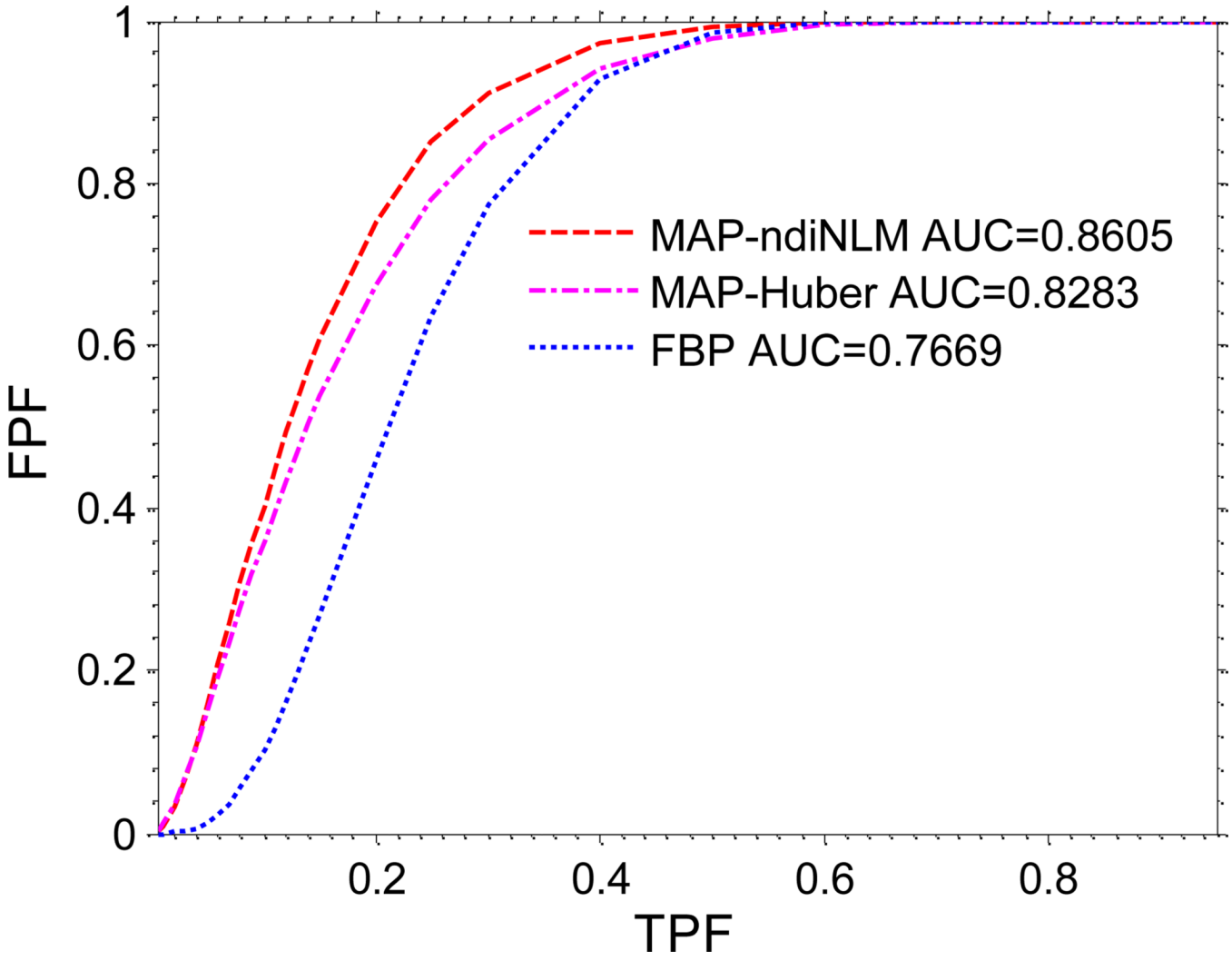

Figure 5.
The ROC curves of the FBP, MAP-Huber, and MAP-ndiNLM methods.

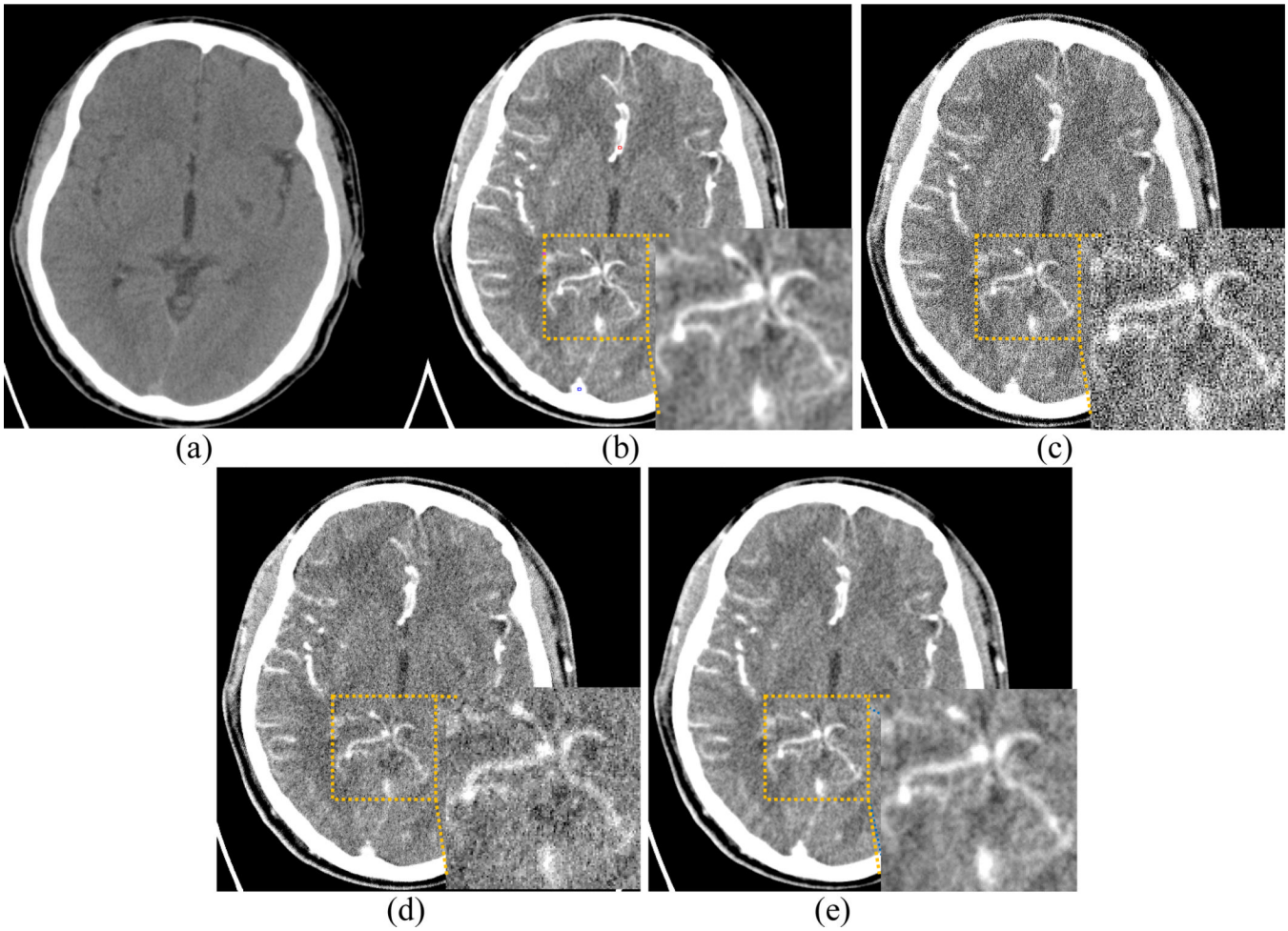

Figure 6.
Cerebral PCT image reconstructions by different methods from the simulated low-dose singoram data. (a) the pre-contrast unenhanced image reconstructed by the FBP method from the pre-contrast normal-dose scan, which acts as the reference image; (b) the image reconstructed by the FBP method from the normal-dose scan; (c) the image reconstructed by the FBP method from the simulated low-dose sinogram data; (d) the image reconstructed by the MAP-Huber method from the simulated low-dose sinogram data ($\beta = 1.0\times10^{3}$); and (e) the image reconstructed by the MAP-ndiNLM method from the simulated low-dose sinogram data (h =80.0, $\beta = 5.0\times10^{-2}$). The display window option: width is 160 HU, level is 56 HU.

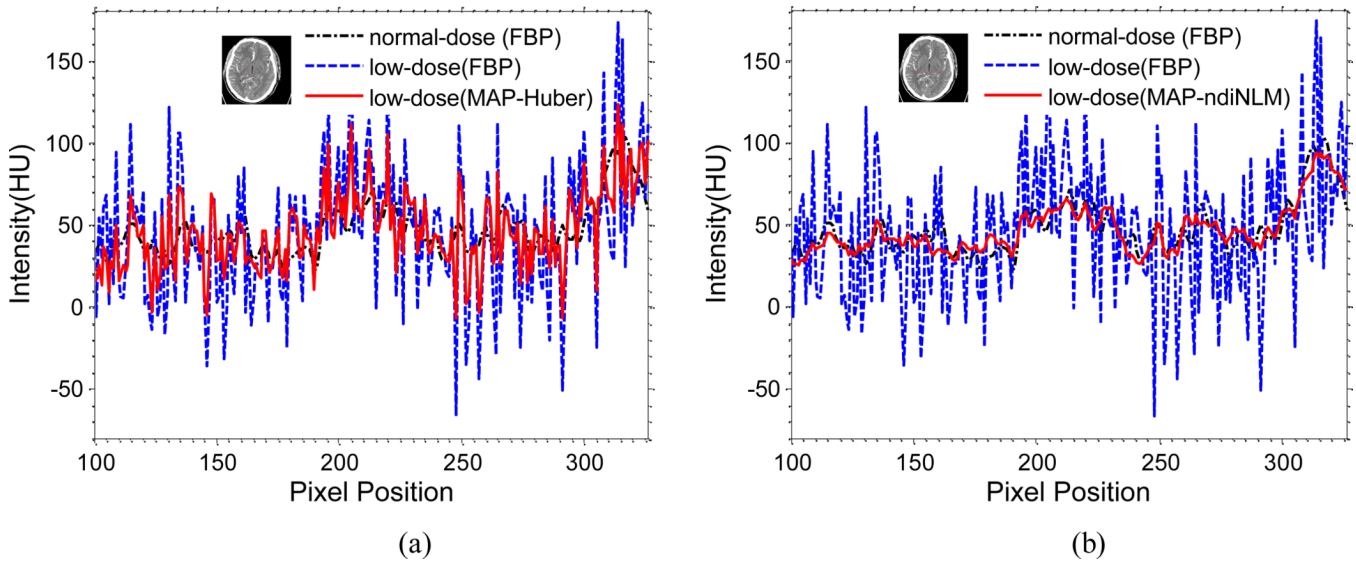

Figure 7.

Horizontal profiles through the center of the images in figure 6. The “blue line” is from the FBP reconstruction while the “red line” is from the reconstructions with the MAP-ndiNLM and MAP-Huber methods, and the “dotted black line” is from the normal-dose image which acts as the ground-truth for comparison.

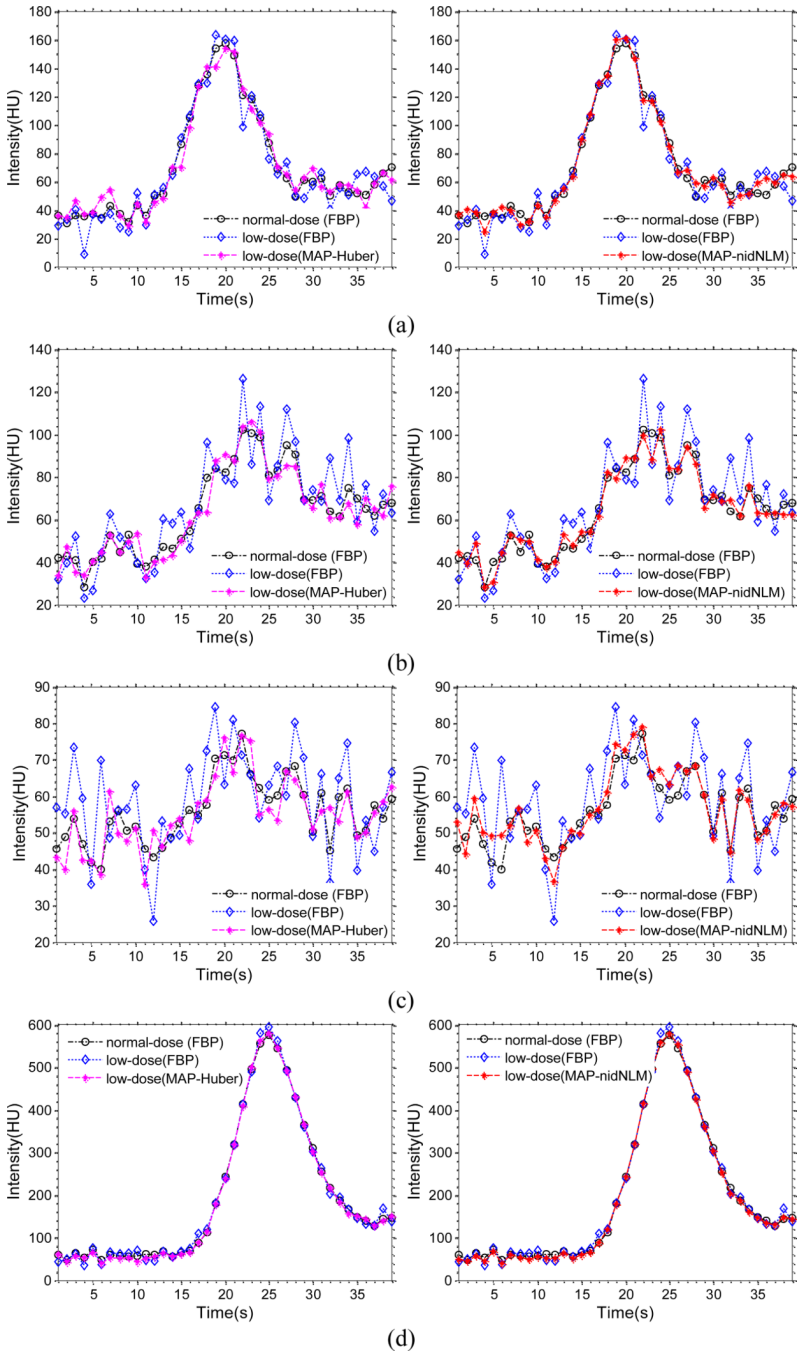

Figure 8.

TDC accuracy of the AIF, VOF and tissue perfusion of dynamic images reconstructed from the noisy sinogram data. (a) TDCs of the AIF (the 3×3 ROI indicated by a red square in Figure 6(b)); (b) TDCs of tissue 1 (the 3×3 ROI indicated by a magenta square in figure 6(b)); (c) TDCs of tissue 2 (the 3×3 ROI indicated by a yellow square in figure 6(b)); and (d) TDCs of the VOF(the 3×3 ROI indicated by a blue square in Figure 6(b)).

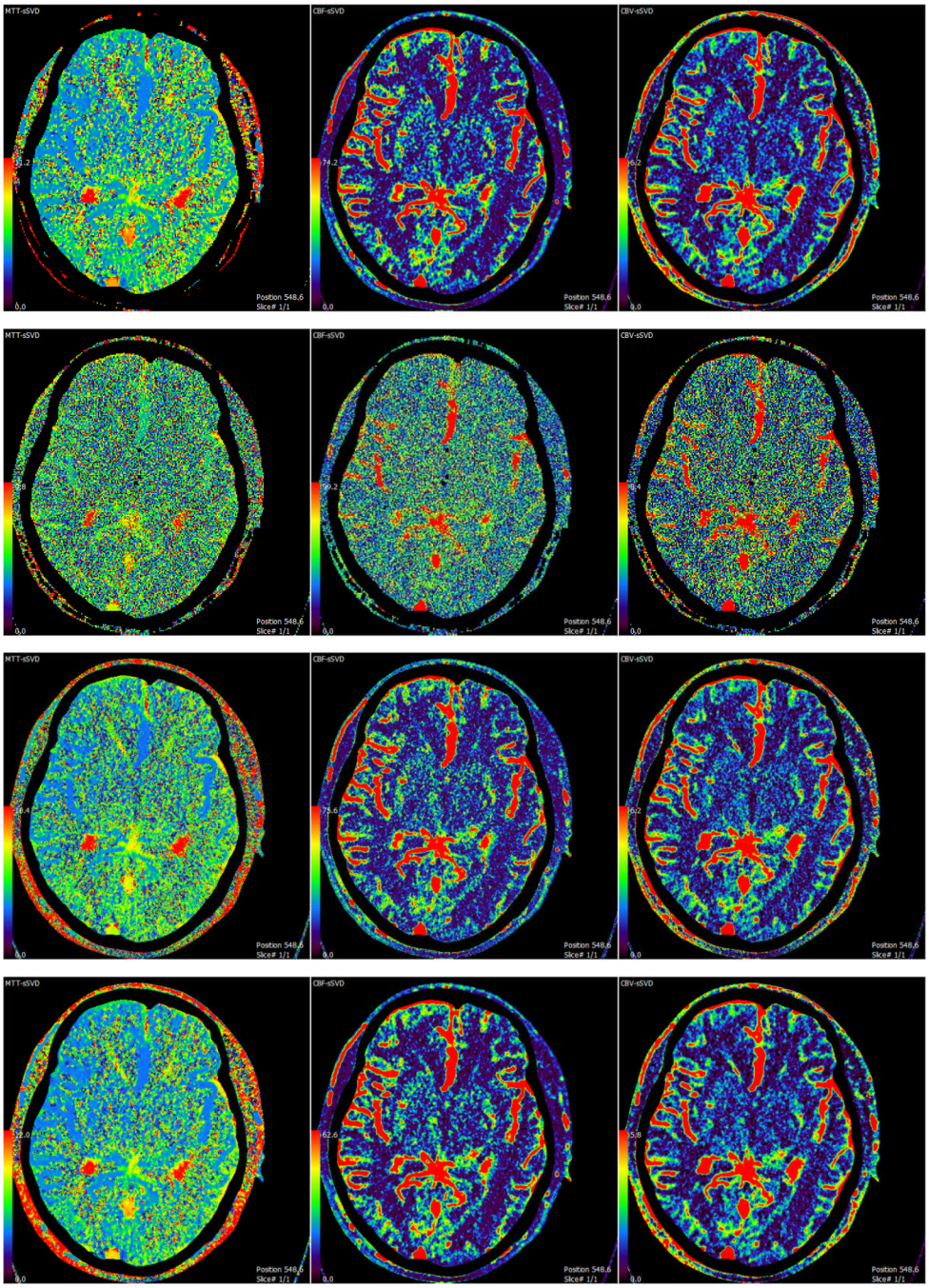

Figure 9.
The MTT (column one), CBF (column two), and CBV (column three) maps calculated from the different brain PCT images. The first row was calculated from the normal-dose images; the second, third and fourth rows were calculated from the simulated low-dose images reconstructed by the FBP, MAP-Huber, and MAP-ndiNLM methods, respectively. The radiation dose in the low-dose sinogram data simulation is about one-seventh of the normal dose.

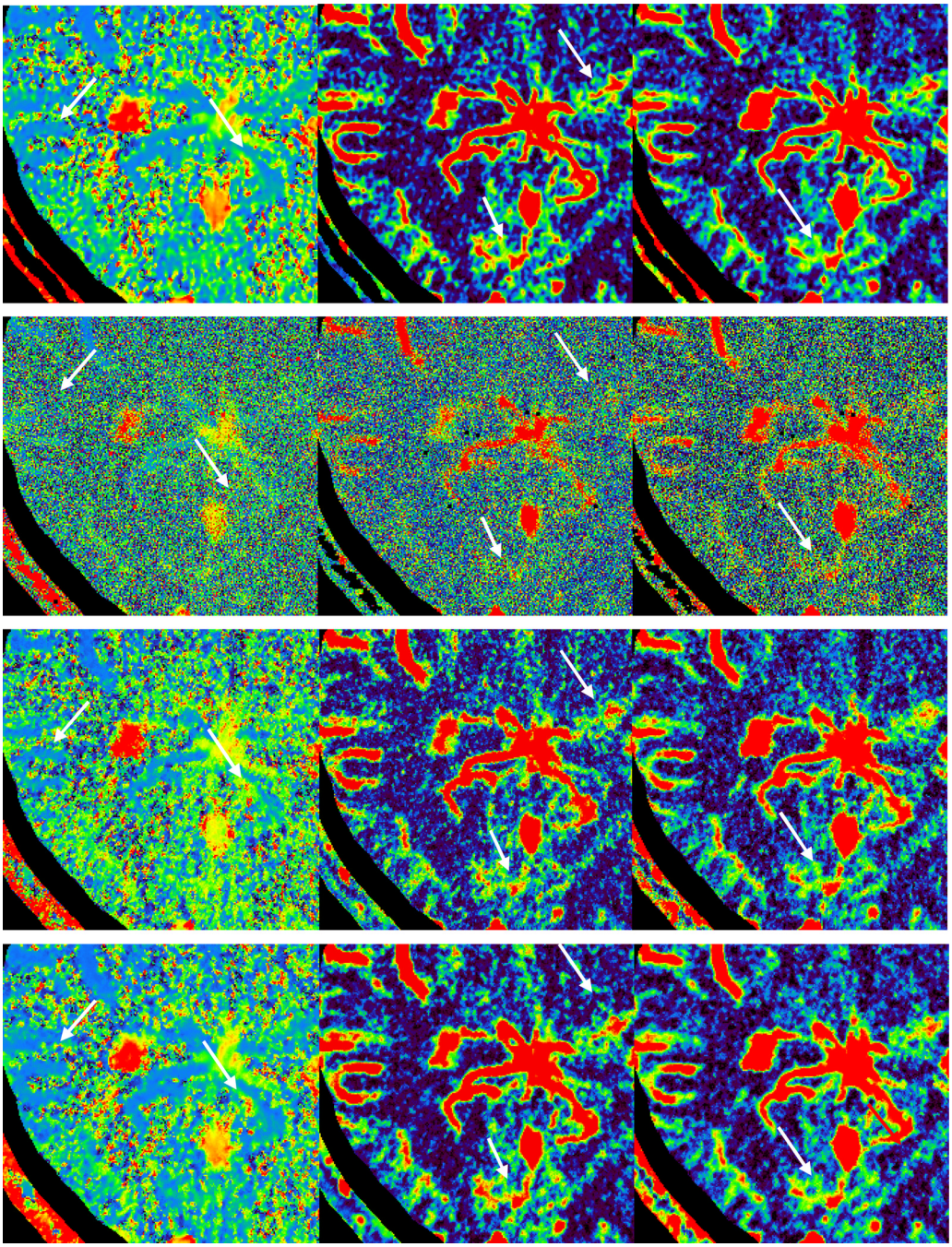

Figure 10.
Zoomed ROIs of the MTT (column one), CBF (column two), and CBV (column three) maps in figure 9. The first row was calculated from the normal-dose images; the second, third and fourth rows were calculated from the simulated low-dose images reconstructed by the FBP, MAP-Huber, and MAP-ndiNLM methods, respectively. The radiation dose in the low-dose sinogram data simulation is about one-seventh of the normal dose.

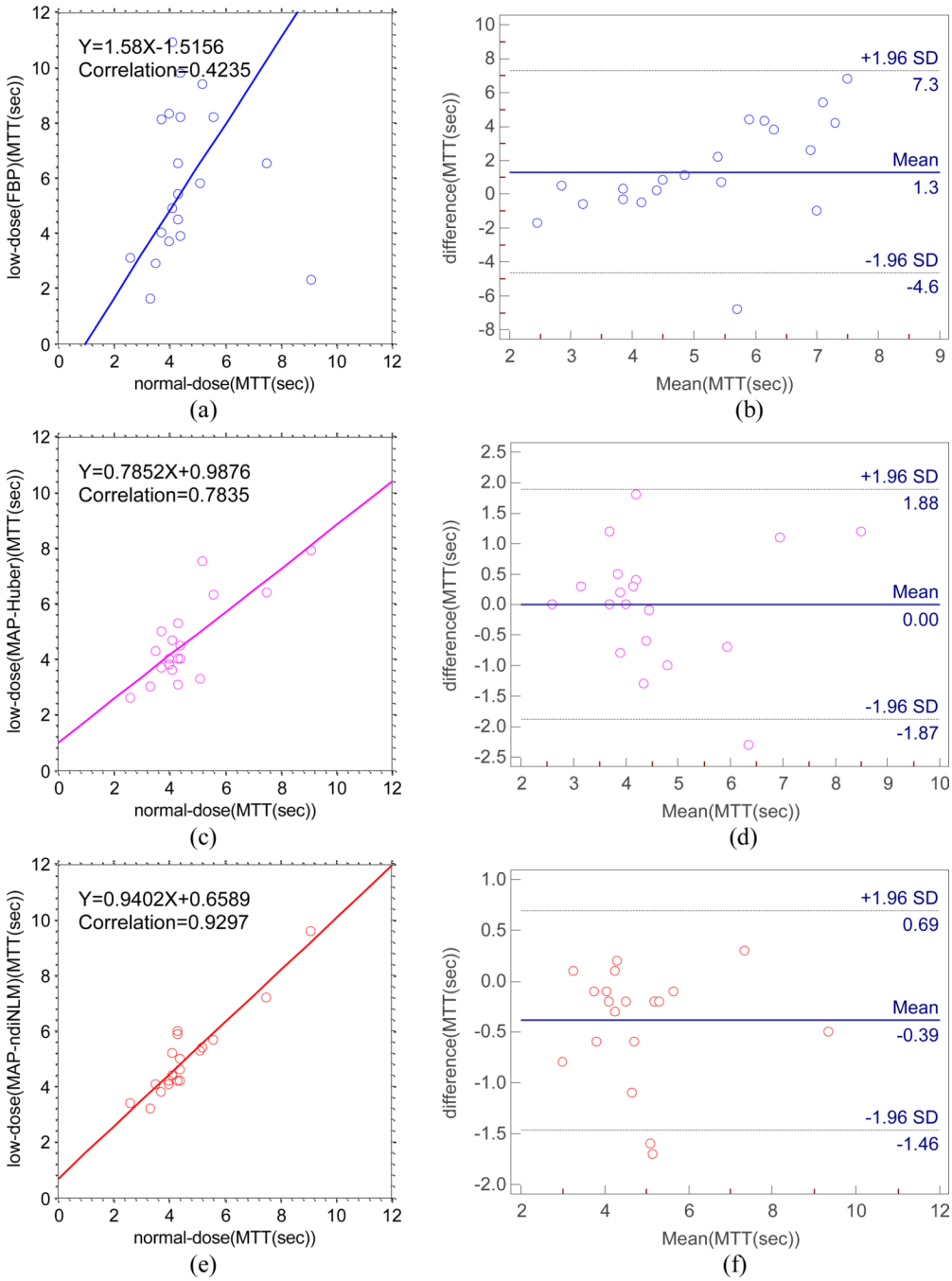

Figure 11.

The correlation (left column) and Bland–Altman plot (right column) between the MTT computed from the normal-dose images and the low-dose images reconstructed by different methods. Plots (a) and (b) represent the results obtained from the normal- and low-dose FBP reconstructions. Plots (c) and (d) represent the corresponding results obtained from the normal-dose images and the low-dose MAP-Huber reconstructions. Plots (e) and (f) represent the corresponding results obtained from the normal-dose images and the low-dose MAP-ndiNLM reconstructions.

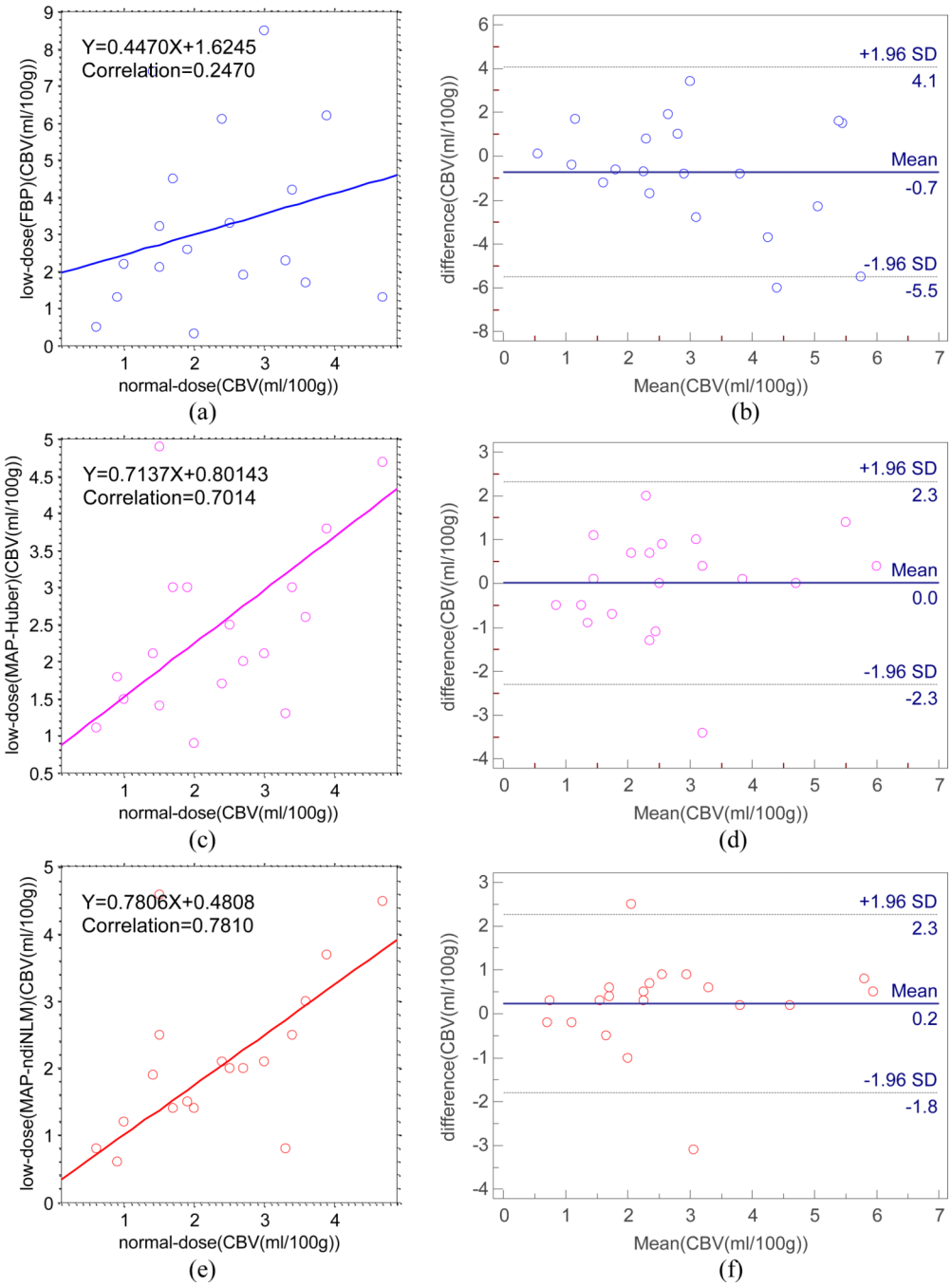

Figure 12.

The correlation (left column) and Bland–Altman plot (right column) between the CBV values computed from the normal-dose images and the low-dose images reconstructed by different methods. Plots (a) and (b) represent the results obtained from the normal- and low-dose FBP reconstructions. Plots (c) and (d) represent the corresponding results obtained from the normal-dose images and the low-dose MAP-Huber reconstructions. Plots (e) and (f) represent the corresponding results obtained from the normal-dose images and the low-dose MAP-ndiNLM reconstructions.

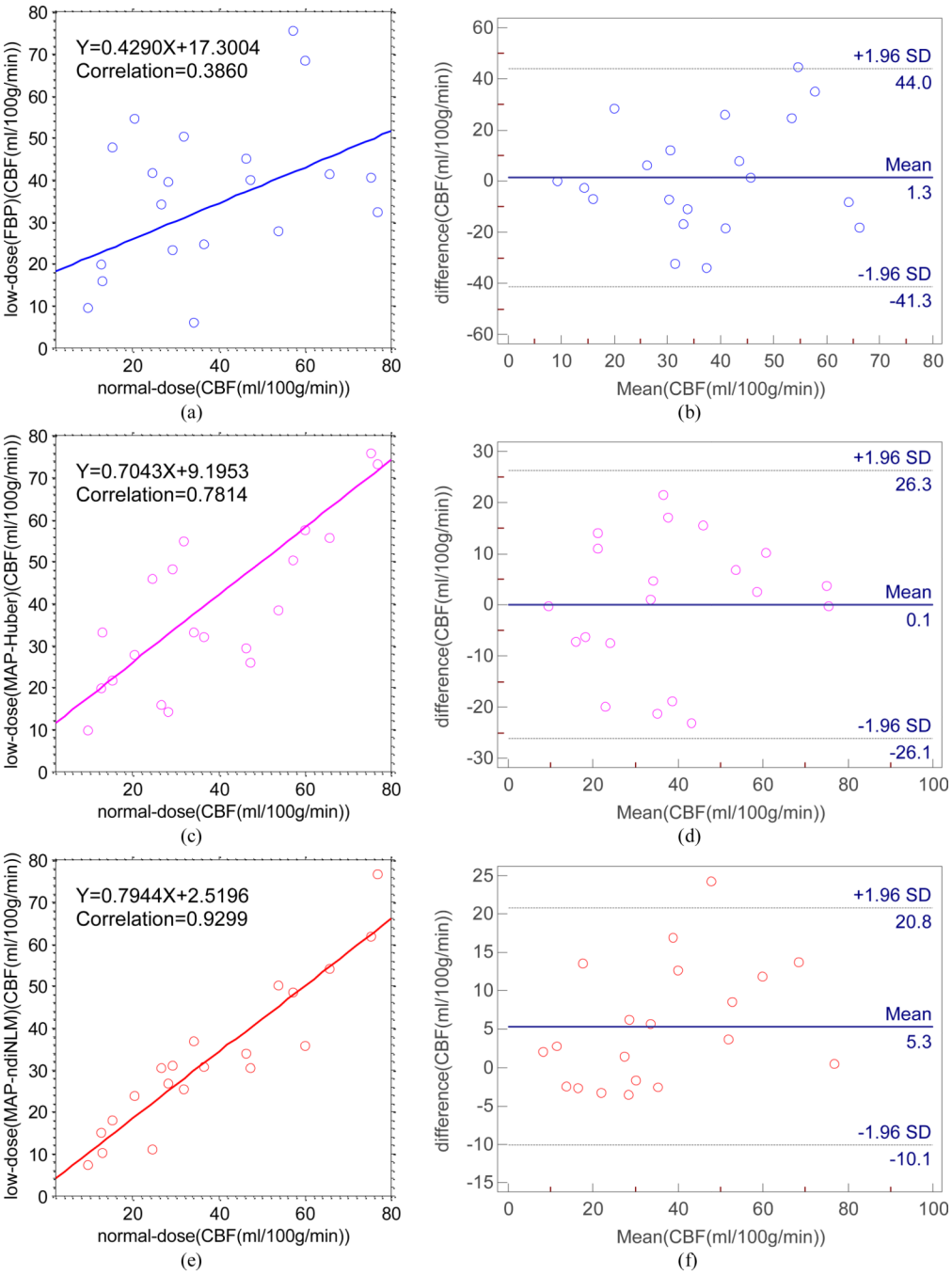

Figure 13.

The correlation (left column) and Bland–Altman plot (right column) between the CBF values computed from the normal-dose images and the low-dose images reconstructed by different methods. Plots (a) and (b) represent the results obtained from the normal- and low-dose FBP reconstructions. Plots (c) and (d) represent the corresponding results obtained from the normal-dose images and the low-dose MAP-Huber reconstructions. Plots (e) and (f) represent the corresponding results obtained from the normal-dose images and the low-dose MAP-ndiNLM reconstructions.

Table 1

Parameters of the modified 2D Shepp-Logan phantom as shown in figure 1(c).

Coordinates of center	Axis lengths	Rotation angles	Intensity
(0.0,0.0)	(0.69,0.92)	90	1200
(0.0,−0.0184)	(0.6224,0.874)	90	−480
(−0.22,0.0)	(0.41,0.16)	108	−120
(0.22,0.0)	(0.31,0.11)	72	−120
(0.0,0.35)	(0.21,0.25)	90	60
(0.0,0.1)	(0.046,0.046)	0	60
(0.0,−0.1)	(0.046,0.046)	0	60
(−0.08,−0.605)	(0.046,0.023)	0	80
(0.0,−0.605)	(0.023,0.023)	0	80
(0.06,−0.605)	(0.046,0.023)	90	80
(0.0,0.61)	(0.029,0.029)	0	36

* Last row of the table lists the parameters of the lesion used in the ROC study.

Table 2

Image quality metrics on the three ROIs indicated by the squares in figure 2(a).

Methods	ROI1			ROI2			ROI3		
	lSNR	MPSE	MPAE	lSNR	MPSE	MPAE	lSNR	MPSE	MPAE
FBP	84.1279	1.2814	1.0280	88.4469	1.1478	0.9249	74.7641	1.3613	1.0921
MAP-Huber	350.9185	0.5796	0.5376	350.6980	0.3392	0.2688	355.0330	0.4324	0.3616
MAP-ndiNLM	375.1192	0.5574	0.4930	547.3539	0.3073	0.2667	431.7086	0.3320	0.2623

Table 3

Lin's concordance correlation coefficient between the TDCs values from the normal-dose images and from the low-dose images reconstructed the by the FBP, MAP-Huber and MAP-ndiNLM methods. The size of each ROI is 3×3 pixels.

ROI	Methods	Sample size N	Lin's concordance correlation coefficient	95% confidence interval of concordance coefficient	p-value of significance level
AIF	FBP	39	0.9712	(0.9455,0.9849)	P<0.0001
	MAP-Huber	39	0.9853	(0.9719,0.9923)	P<0.0001
	MAP-ndiNLM	39	0.9907	(0.9822,0.9952)	P<0.0001
VOF	FBP	39	0.9982	(0.9966,0.9991)	P<0.0001
	MAP-Huber	39	0.9997	(0.9994,0.9998)	P<0.0001
	MAP-ndiNLM	39	0.9997	(0.9994,0.9998)	P<0.0001
Tissue1	FBP	39	0.9015	(0.8188,0.9475)	P<0.0001
	MAP-Huber	39	0.9572	(0.9193 ,0.9775)	P<0.0001
	MAP-ndiNLM	39	0.9755	(0.9535,0.9872)	P<0.0001
Tissue2	FBP	39	0.6750	(0.4568,0.8166)	P<0.0001
	MAP-Huber	39	0.8611	(0.7491,0.9252)	P<0.0001
	MAP-ndiNLM	39	0.9261	(0.8627,0.9609)	P<0.0001